This is the author's version of an article that has been published in the IROS 2021 proceedings.
Changes were made to this version by the publisher prior to publication.
The final version of record is available at https://doi.org/10.1109/IROS51168.2021.9636447

A Parameter Identification Method for Static Cosserat Rod Models: Application to Soft Material Actuators with Exteroceptive Sensors

Max Bartholdt[2*], Mats Wiese[1*], Moritz Schappler[2], Svenja Spindeldreier[2] and Annika Raatz[1]

***Abstract*— Soft material robotics is a rather young research field in the robotics and material science communities. A popular design is the soft pneumatic actuator (SPA) which, if connected serially, becomes a highly compliant manipulator. This high compliance makes it possible to adapt to the environment and in the future might be very useful for manipulation tasks in narrow and wound environments. A central topic is the modelling of the manipulators. While comparatively rigid continuum robots are build of metal or other materials, that conduct a linear behaviour, the material used in soft material robotics often exhibits a nonlinear stress-strain relationship. In this paper we contribute an identification method for material parameters and data-based approach within the constitutive equations of a Cosserat rod model. We target bending and extension stiffness, consider shear and neglect torsional strains. The proposed method is applicable to any continuum robot which can be modelled by the classic theory of special Cosserat rods, including constraint models, and shows great improvement in experimental results with mean position errors of 0.59% reference length.**

I. INTRODUCTION

Geometrically exact beam and rod theories such as the special Cosserat rod theory play a central role in modelling continuum robots. They have been applied in feed-forward control strategies [1], design optimisation [2] as well as in simulations [3]. The Cosserat rod model considers shear, extension and flexure as well as torsion. In the young field of soft material robotics, the ability to account for nonlinear material effects in large deformations and shearing deformation is of importance [4], [5], [6]. In [7] pneumatic, McKibben-like actuators are modelled as cylindric, hyperelastic continua and forces induced by the actuator are applied to a Cosserat rod model, although the manipulator itself is realised without a backbone structure. However, the material law of the rod is modelled as linear elasticity. Nonlinear effects in stiffness due to coupling of asymmetric fibre reinforced entangled enclosures have experimentally been shown by [8]. An identification method is presented using a constraint optimisation of four parameters, whereof two are material parameters and two kinematic parameters. For the optimisation process the shape of the manipulator is measured utilising a scan arm. The applied model of the static rod contains flexure and torsion under the assumption of a constant curvature and torsion due to the internal pressure. They are treated as kinematic parameters and optimised for every tuple of pressure.

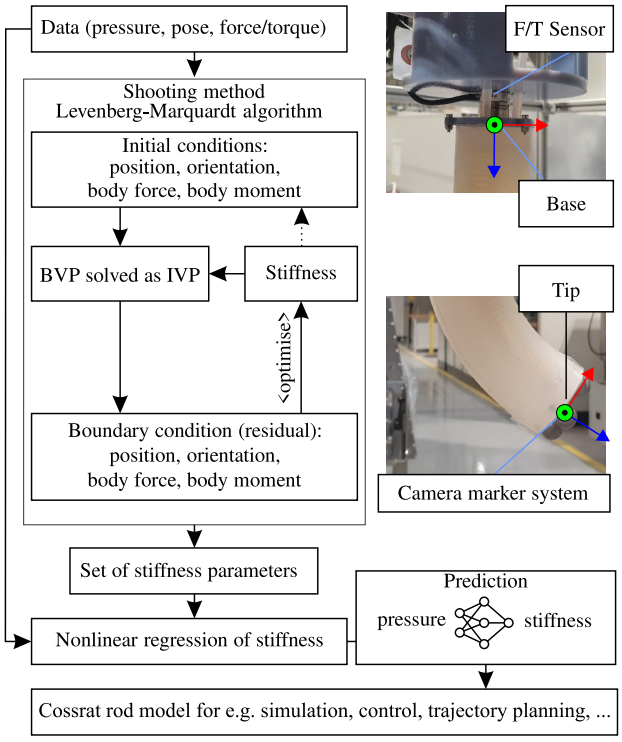

Fig. 1. Overview of the identification procedure. The boundary value problem (BVP) of the rod is solved with a shooting method as initial value problem (IVP)(optimisation of stiffness parameter, or optional initial conditions if they are not measured). The pictures on the right hand side show the actuator and sensor systems utilised, to measure the boundary condition at the base and tip. As a result a map of linear stiffness parameters is exported and used to train artificial neuronal networks.

A popular soft pneumatic actuator design with three symmetric, cylindrical air chambers was experimentally examined regarding the modelling with Cosserat rod beams [9]. Gilbert et al. state, that qualitative results of their dynamic model are promising, but errors due to manufacturing and material nonlinearity need to be considered. The drawback of Cosserat rod models lies within the computation time, if compared to multi-body models based on the constant curvature kinematic like the ones used in [10] and [11]. Moreover, the authors of [1] state that in order to perform static feedback control, rod models do not improve performance due to a manifold of unknown system parameters and

*Both authors contributed equally to this publication.

[1,2]All authors are with the Leibniz University Hannover, Germany.
[1]Authors are with the Institute of Assembly Technology wiese@match.uni-hannover.de
[2]Authors are with the Institute of Mechatronic Systems max.bartholdt@imes.uni-hannover.de

Funded by the Deutsche Forschungsgemeinschaft (DFG, German Research Foundation) under grant no. 405032969.

strong model order reduction, which is necessary to reach a sufficient computational time. They base their conclusion on the results of a comparative study in [12].

Recent advances have shown that with certain numerical models and efficient implementation, a computation time below 10 ms for Cosserat rod models considering system dynamics with over 100 spatial nodes is possible [3]. Till et al. present different actuator concepts and provide corresponding modelling strategies, validating the models for slender continuum robots or rods. Also, finite element approaches used on Cosserat rod theory have been implemented that show great improvement in computational time and resulted in the SimSOFT environment [13].

This contribution follows these advances and proposes a method to improve the precision of the models when used in an application. Computational efficiency is maintained by targeting the constitutive equations of elasticity. By this problems discussed in [1] and [9] are targeted with a hybrid modelling approach. In this study, sole static models based on the numerical integration schemes given in [3] are investigated.

The overall idea, depicted in Fig. 1, is to identify model parameters, in this case the stiffness parameters, by measuring the boundary conditions (BC) of an actuator segment. For each static point measured, an optimisation of the constitutive parameters and optionally unknown boundary conditions takes place, generating a stiffness map.

Artificial neural networks are used as nonlinear regression method to estimate the stiffness for different combinations of pressure. The proposed method is applicable to any Cosserat beam model using linear material laws, improving their accuracy when applied to real systems. In contrast to model-free machine learning approaches as in [14], a straight forward transition to dynamic and contact modelling and simulation is possible.

To summarise, the contributions of this paper are

- a theoretical concept for the material parameter identification of Cosserat rod models using heterogeneous exteroceptive measurements as boundary conditions,
- the incorporation of identified parameters in hybrid modelling (i.e. combination of classical modelling schemes and data based approaches),
- the exemplary application of the general concept to a soft pneumatic actuator,
- experimental validation of the method using an external camera system for end effector tracking.

The remainder of the paper is structured as follows. Sec. II summarises the analytical and numerical model composed of three serial beams with boundary conditions at each transition. The single segment actuator is briefly reviewed and all geometrical assumptions are explained. Thereafter, in Sec. III, details on the optimisation problem, possible cost functions and the applied topology of the artificial neuronal networks for nonlinear regression of the optimisation results are given. Sec. IV outlines the experimental setup including sensors, actuators as well as software for data acquisition and control. The described methods are then validated and discussed with an SPA test bench in Sec. V. Sec. VI concludes the paper.

II. MODELLING: THEORETICAL BACKGROUND

Fig. 2 depicts the outer view and the cross sectional view of the soft pneumatic actuator that is considered in this paper.

The actuator has a total length of 130 mm. The middle section is made of Ecoflex00-50 silicone, while the caps consist of the stiffer Dragon Skin 20 silicone (Smooth-On, Inc.). The three pressure chambers are fibre reinforced to prevent radial expansion when pressurised.

The actuator is modelled using a static Cosserat rod model. For the basic model, the following assumptions apply:

- The material exhibits a linear elastic behaviour.
- The deformed cross sections are approximated by tangential planes at the centerline.
- Reinforcing fibres are not explicitly modelled but considered by the assumption of a constant chamber cross section under deformation.
- Pressure acting on the lateral chamber walls is neglected.
- Geometrical dimensions of the design apply to manufactured actuators.

In the following, we briefly review the basic kineto-static relations for the special Cosserat rod theory with linear elastic materials. Detailed derivations can be found in [15]. Subsequently, the model is specified to include the pneumatic actuation and boundary conditions for the considered SPA. The notation follows [15] and [3].

A. Kinematics

The macroscopic deformation of the actuator is described by a one dimensional backbone curve with an initial length L and a centerline $\boldsymbol{r}(s) \in \mathbb{R}^3$, where s is the arc length parameter in the undeformed state. The curve's orientation is given by a rotation matrix $\boldsymbol{R}(s) \in \mathrm{SO}(3)$. For the sake of clarity, the dependency of s in the following equations

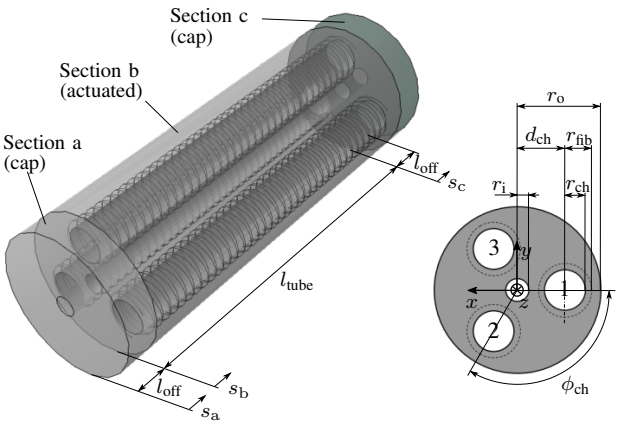

Fig. 2. Outer view and cross section (as seen from clamped side) of soft pneumatic actuator under investigation. s_{a}, s_{b} and s_{c} denote the arc length parameter per section a, b and c. The cross sectional view also depicts the numeration of the pressure chambers.

TABLE I
PARAMETERS OF THE SOFT PNEUMATIC ACTUATOR

parameters	l_{tube}	l_{off}	r_{o}	r_{i}
value	110 mm	10 mm	21.1 mm	2.9 mm
parameter	r_{ch}	d_{ch}	r_{fib}	ϕ_{ch}
value	5.15 mm	12 mm	6.7 mm	120°
parameter	ρ_{EF}	ρ_{DS}	E_{EF}	E_{DS}
value	1070 $\frac{\text{kg}}{\text{m}^3}$	1080 $\frac{\text{kg}}{\text{m}^3}$	82.7 kPa	337.8 kPa

is left out after the variable first appeared in the text. The rate of change of position $\boldsymbol{v}(s)$ in the local frame and the flexure and torsional strains $\boldsymbol{u}(s)$ in the local frame can be calculated with

$$\boldsymbol{v} = \boldsymbol{R}^{\mathrm{T}}\boldsymbol{r}_s \quad \text{and} \quad \hat{\boldsymbol{u}} = \boldsymbol{R}^{\mathrm{T}}\boldsymbol{R}_s, \tag{1}$$

where $()_s$ indicates the derivative w.r.t. arclength s. The $\hat{}$-operator denotes a transformation from a vector to a skew-symmetric matrix.

B. Statics and Material Law

For a mechanical model the equilibrium of forces and moments in the global frame is formulated for infinitesimal sections along the arc length, yielding

$$\begin{aligned} \boldsymbol{n}_s + \boldsymbol{f} &= \boldsymbol{0} \\ \boldsymbol{m}_s + \boldsymbol{r}_s \times \boldsymbol{n} + \boldsymbol{l} &= \boldsymbol{0}, \end{aligned} \tag{2}$$

with $\boldsymbol{n}(s)$ and $\boldsymbol{m}(s)$ denoting the body force and moment, respectively, and $\boldsymbol{f}(s)$ and $\boldsymbol{l}(s)$ the distributed forces and moments.

In the linear elastic case, the local change of position is related to body forces at a material point s and the stiffness $\boldsymbol{K}_{\text{se}} = \text{diag}(GA, GA, EA)$ (shear (s), extension (e)). Analogously, the local flexural and torsional strains are dependent on the body moment and the respective stiffness $\boldsymbol{K}_{\text{bt}} = \text{diag}(EI_x, EI_y, GI_z)$ (bending (b) or twist (t)) with shear modulus G, elastic modulus E, cross sectional area A and second moment of area I resulting in

$$\begin{aligned} \boldsymbol{v} &= \boldsymbol{K}_{\text{se}}^{-1}\boldsymbol{R}^{\mathrm{T}}\boldsymbol{n} + \boldsymbol{v}^* \\ \boldsymbol{u} &= \boldsymbol{K}_{\text{bt}}^{-1}\boldsymbol{R}^{\mathrm{T}}\boldsymbol{m} + \boldsymbol{u}^*. \end{aligned} \tag{3}$$

The symbols $\boldsymbol{v}^*(s)$ and $\boldsymbol{u}^*(s)$ specify the initial configuration. In case of a straight rod pointing in z-direction $\boldsymbol{v}^* = \begin{pmatrix}0 & 0 & 1\end{pmatrix}^{\mathrm{T}}$ and $\boldsymbol{u}^* = \boldsymbol{0}$ apply. Rearranging (1) to (2) and combining with (3) yields a system of ordinary differential equations (ODE)

$$\begin{aligned} \boldsymbol{r}_s &= \boldsymbol{R}\boldsymbol{v} \\ \boldsymbol{R}_s &= \boldsymbol{R}\hat{\boldsymbol{u}} \\ \boldsymbol{n}_s &= -\boldsymbol{f} \\ \boldsymbol{m}_s &= -\boldsymbol{r}_s \times \boldsymbol{n} - \boldsymbol{l} \end{aligned} \tag{4}$$

that can be solved by defining boundary conditions and performing numerical integration.

C. Application to a Soft Pneumatic Actuator

As explained in [3], the Cosserat rod model applied to the soft pneumatic actuator includes distributed forces $\boldsymbol{f}_{\text{p}}(s)$ and moments $\boldsymbol{l}_{\text{p}}(s)$ that are induced by the actuating pressures and gravitational forces $\boldsymbol{f}_{\text{g}}$ with gravity vector $\boldsymbol{g}$, yielding

$$\boldsymbol{f} = \boldsymbol{f}_{\text{g}} - \boldsymbol{f}_{\text{p}} = \rho A \boldsymbol{g} - \sum_{i=1}^{M=3} p_i A_{\text{c},i} \boldsymbol{R}_s \vec{\boldsymbol{e}}_z \tag{5}$$

$$\boldsymbol{l} = -\sum_{i=1}^{M=3} p_i A_{\text{ch},i} \boldsymbol{R}_s \left[(\boldsymbol{v} + \hat{\boldsymbol{u}}\boldsymbol{d}_{\text{ch},i}) \times \vec{\boldsymbol{e}}_z + \boldsymbol{d}_{\text{ch},i} \times \hat{\boldsymbol{u}}\vec{\boldsymbol{e}}_z\right]. \tag{6}$$

Within the model, the actuating air pressure p_i acts on the top and bottom surface $A_{\text{ch},i} = \pi r_{\text{ch}}^2$ of chamber i with orthonormal vector $\vec{\boldsymbol{e}}_z$. For the distributed moment $\boldsymbol{l}$ the pressure-induced force is multiplied with lever $\boldsymbol{d}_{\text{ch},i}$ as the center of the corresponding chamber cross section, relative to the segment's center line expressed in the local frame. Note that distributed forces and moments caused by the difference in effective area from the outer and inner lateral surface of each chamber, while being deformed, are neglected.

For reasons of numerical stability and following [16], a quaternion representation $\boldsymbol{h}(s)$ for the orientation of the rod instead of the rotation matrix is used. For the sake of simplicity in the following equations, the state variables are summarised as $\boldsymbol{y} = \begin{pmatrix}\boldsymbol{r}^{\mathrm{T}} & \boldsymbol{h}^{\mathrm{T}} & \boldsymbol{n}^{\mathrm{T}} & \boldsymbol{m}^{\mathrm{T}}\end{pmatrix}^{\mathrm{T}}$.

The actuator is comprised of three sections, namely the actuated Ecoflex section and Dragon Skin caps (refer to Fig. 2). Therefore, the model consists of three beams (a/b/c) with states variables $\boldsymbol{y}(s_{\text{a}})$, $\boldsymbol{y}(s_{\text{b}})$ and $\boldsymbol{y}(s_{\text{c}})$ that are coupled at their ends with

$$\begin{aligned} \boldsymbol{y}(s_{\text{a}} = 0) &= \boldsymbol{y}_{\text{a0}} & \boldsymbol{y}(s_{\text{a}} = l_{\text{off}}) &= \boldsymbol{y}_{al} \\ \boldsymbol{y}(s_{\text{b}} = 0) &= \boldsymbol{y}_{\text{b0}} & \boldsymbol{y}(s_{\text{b}} = l_{\text{tube}}) &= \boldsymbol{y}_{\text{b}l} \\ \boldsymbol{y}(s_{\text{c}} = 0) &= \boldsymbol{y}_{\text{c0}} & \boldsymbol{y}(s_{\text{c}} = l_{\text{off}}) &= \boldsymbol{y}_{\text{c}l}. \end{aligned} \tag{7}$$

For the coupling points, $\boldsymbol{y}_{\text{b0}} = \boldsymbol{y}_{al}$ and $\boldsymbol{y}_{\text{c0}} = \boldsymbol{y}_{\text{b}l}$ holds for position and material orientation. Due to the actuating pressure in section b there is a discontinuity in force and moment, giving

$$\begin{aligned} \boldsymbol{n}_{\text{b0}} &= \boldsymbol{n}_{al} + \sum_{i=1}^{M=3} p_i A_{\text{ch},i} \boldsymbol{R}_{\text{b0}} \vec{\boldsymbol{e}}_z \\ \boldsymbol{m}_{\text{b0}} &= \boldsymbol{m}_{al} + \sum_{i=1}^{M=3} \hat{\boldsymbol{d}}_{\text{ch},i} p_i A_{\text{ch},i} \boldsymbol{R}_{\text{b0}} \vec{\boldsymbol{e}}_z \end{aligned} \tag{8}$$

and

$$\begin{aligned} \boldsymbol{n}_{\text{c0}} &= \boldsymbol{n}_{\text{b}l} - \sum_{i=1}^{M=3} p_i A_{\text{ch},i} \boldsymbol{R}_{\text{c0}} \vec{\boldsymbol{e}}_z \\ \boldsymbol{m}_{\text{c0}} &= \boldsymbol{m}_{\text{b}l} - \sum_{i=1}^{M=3} \hat{\boldsymbol{d}}_{\text{ch},i} p_i A_{\text{ch},i} \boldsymbol{R}_{\text{c0}} \vec{\boldsymbol{e}}_z. \end{aligned} \tag{9}$$

The ODE system in (4) is treated as a boundary value problem (BVP) with boundary conditions given by a fixed clamped side, thus $\boldsymbol{r}_{\text{a0}} = \boldsymbol{0}$ and $\boldsymbol{h}_{\text{a0}} = \begin{pmatrix}1 & 0 & 0 & 0\end{pmatrix}^{\mathrm{T}}$. If no additional load is acting on the free end of the actuator the body forces and moments at that point vanish, meaning $\boldsymbol{n}_{\text{c}l} = \boldsymbol{0}$ and $\boldsymbol{m}_{\text{c}l} = \boldsymbol{0}$.

D. Numeric Model

For simulation of an actuator we solve the BVP by applying a shooting method as described in [3]. Therefore, the rod is discretised into $N+1$ nodes. The rod's base and tip are denoted by indices 0 and N. Boundary conditions are accounted for by setting $\boldsymbol{r}_0 = \boldsymbol{r}_{\mathrm{a}0}$ and $\boldsymbol{h}_0 = \boldsymbol{h}_{\mathrm{a}0}$. In combination with an initial guess for the body forces $\boldsymbol{n}_0$ and $\boldsymbol{m}_0$ the state $\boldsymbol{y}$ is numerically integrated along the actuator using the fourth order Runge-Kutta method. The residual e at the actuator's tip is calculated with

$$e = \left\| \begin{pmatrix} (\boldsymbol{n}_{\mathrm{cl}} - \boldsymbol{n}_N)^{\mathrm{T}} & (\boldsymbol{m}_{cl} - \boldsymbol{m}_N)^{\mathrm{T}} \end{pmatrix}^{\mathrm{T}} \right\|_2^2. \tag{10}$$

The Levenberg-Marquardt algorithm is used to minimise the residual by updating $\boldsymbol{n}_0$ and $\boldsymbol{m}_0$ accordingly as

$$\begin{pmatrix} \boldsymbol{n}_0^{*\mathrm{T}} & \boldsymbol{m}_0^{*\mathrm{T}} \end{pmatrix}^{\mathrm{T}} = \underset{\boldsymbol{n}_0, \boldsymbol{m}_0}{\arg\min}\, e(\boldsymbol{n}_0, \boldsymbol{m}_0). \tag{11}$$

Thereby, the discretised state $\boldsymbol{y}$ along the Cosserat rod is determined to yield the configuration of the SPA model. In the next section, the initial conditions and residual e are adapted to contain more boundary conditions and the targeted optimisation variables are switched to the rod's stiffness parameters.

III. HYBRID MODELLING

The hybrid modelling approach combines parameter identification of a physical model with artificial neuronal networks learning these parameter sets. To generate the required stiffness data for learning, the previously presented optimisation problem can be reformulated in terms of the optimisation variables. If additional boundary conditions at one end of the rod for a static configuration are measured, it is possible to optimise the parameters of the chosen inverse material law, which is mapping the local body forces and moments to local displacements.

For the presented actuator, an operating-point-dependent linear material law is introduced. On the one hand, compared to a nonlinear material law, this approach provides higher computational efficiency, since displacements may be calculated by inverting a stiffness matrix instead of solving a set of nonlinear equations. On the other hand, if chosen and identified correctly, a nonlinear material law would possibly lead to more precise estimation of the configuration, which is the whole body deformation of the actuator.

A. Identification of Stiffness Characteristics

An operating-point-dependent linear material law implies linearising a nonlinear material law $\boldsymbol{v} = \bar{\boldsymbol{v}}(\boldsymbol{n})$ $[\boldsymbol{u} = \bar{\boldsymbol{u}}(\boldsymbol{m})]$ for an operating point $\boldsymbol{n}^\circ$ $[\boldsymbol{m}^\circ]$ resulting in

$$\boldsymbol{v} = \left.\frac{\partial \bar{\boldsymbol{v}}(\boldsymbol{n})}{\partial \boldsymbol{n}}\right|_{\boldsymbol{n}^\circ} \boldsymbol{n} \quad \text{and} \quad \boldsymbol{u} = \left.\frac{\partial \bar{\boldsymbol{u}}(\boldsymbol{m})}{\partial \boldsymbol{m}}\right|_{\boldsymbol{m}^\circ} \boldsymbol{m}. \tag{12}$$

Finding the hypotheses $\bar{\boldsymbol{v}}$ and $\bar{\boldsymbol{u}}$ that sufficiently describe the reality in this case, is cumbersome. Challenging fabrication techniques result in anisotropic properties of the actuator and deviation from the assumed geometry described in the previous section. Furthermore, the compressible medium will affect the stiffness as well.

Therefore, in this first study, we assume the inverse material law to be dependent on the pressure within the chambers and to be described by the algebraic equations

$$\begin{aligned} \boldsymbol{v}(s, \boldsymbol{p}) &= \boldsymbol{K}_{\mathrm{se}}^{-1}(\boldsymbol{p}) \left[\boldsymbol{R}^{\mathrm{T}} \boldsymbol{n}(s)\right] + \boldsymbol{v}^*, \\ \boldsymbol{u}(s, \boldsymbol{p}) &= \boldsymbol{K}_{\mathrm{bt}}^{-1}(\boldsymbol{p}) \left[\boldsymbol{R}^{\mathrm{T}} \boldsymbol{m}(s)\right] + \boldsymbol{u}^*. \end{aligned} \tag{13}$$

By repeating the parameter optimisation for multiple deformation states, a table of stiffness values for each degree of freedom of deformation is generated. The deformation in our case is caused by the distributed body forces and moments induced by pressure within the chambers. Since shear load is small compared to bending moments and normal forces, we here rely on literature parameters given in Tab. I. For an explanation of geometric parameters refer to Fig. 2. ρ_{EF} and ρ_{DS} denote the density of Ecoflex00-50 and Dragon Skin 20, respectively. E_{EF} and E_{DS} are the respective elastic moduli according to the manufacturer.

For this identification procedure the twist, described by the component u_z, is constrained to be zero, since for all load cases in the model $m_z = 0$. This way a triple (EA, EI_x, EI_y) for each triple of (p_1, p_2, p_3) is identified. Thereby, errors in the mapping of pressure to normal forces and moments are taken into account.

B. Optimisation Problem

The cost function subject to minimisation is the residual e between the boundary conditions and the result of the numeric integration method. Both directions of integration either tip to base or base to tip are possible.

The residual is defined by a combination of differences

$$\boldsymbol{e}_{\boldsymbol{r}} = \boldsymbol{r}_* - \boldsymbol{r}_N, \tag{14}$$

$$\boldsymbol{e}_{\boldsymbol{R}} = \Phi(\log(\boldsymbol{R}_N^{\mathrm{T}} \boldsymbol{R}_*)), \tag{15}$$

$$\boldsymbol{e}_{\boldsymbol{n}} = \boldsymbol{n}_* - \boldsymbol{n}_N, \tag{16}$$

$$\boldsymbol{e}_{\boldsymbol{m}} = \boldsymbol{m}_* - \boldsymbol{m}_N, \tag{17}$$

where the index $*$ is a placeholder for the BC at tip or base, N describes the N-th and thereby last node of the numeric integration. The operator Φ maps the skew-symmetric matrix as result of the matrix logarithm to $\boldsymbol{e}_{\boldsymbol{R}} \in \mathbb{R}^3$ as axis-angle-representation of the rotation between $\boldsymbol{R}_N$ and $\boldsymbol{R}_*$ [17].

In order to accomplish comparability of the different physical quantities in $\boldsymbol{e}_{\boldsymbol{r}}$, $\boldsymbol{e}_{\boldsymbol{R}}$, $\boldsymbol{e}_{\boldsymbol{m}}$ and $\boldsymbol{e}_{\boldsymbol{n}}$, two virtual, translational and rotational springs at the node N transfer displacements, forces and moments into energy. This potential energy is used to compare the deviation in force, moments, deviation in position or orientation. For the translational stiffness it is defined by

$$U_{\mathrm{tc},1} = \frac{c_{\mathrm{t}}}{2} \boldsymbol{e}_{\boldsymbol{r}}^{\mathrm{T}} \boldsymbol{e}_{\boldsymbol{r}} \quad \text{and} \quad U_{\mathrm{tc},2} = \frac{c_{\mathrm{t}}}{2} \left(\frac{\boldsymbol{e}_{\boldsymbol{n}}^{\mathrm{T}} \boldsymbol{e}_{\boldsymbol{n}}}{c_{\mathrm{t}}^2} \right), \tag{18}$$

and for the rotational stiffness by

$$U_{\mathrm{rc},1} = \frac{c_{\mathrm{r}}}{2} \boldsymbol{e}_{\boldsymbol{R}}^{\mathrm{T}} \boldsymbol{e}_{\boldsymbol{R}} \quad \text{and} \quad U_{\mathrm{rc},2} = \frac{c_{\mathrm{r}}}{2} \left(\frac{\boldsymbol{e}_{\boldsymbol{m}}^{\mathrm{T}} \boldsymbol{e}_{\boldsymbol{m}}}{c_{\mathrm{r}}^2} \right), \tag{19}$$

The spring's stiffness c_t is determined by

$$c_\mathrm{t} = \frac{n_\mathrm{high}}{r_\mathrm{high}} \tag{20}$$

and has the same value for both translational springs. The two scalars n_high and r_high in the fraction are values for force and position empirically weighted as high deviation from the measured or assumed BC, so that for a high deviation each virtual spring stores the same amount of energy. The same procedure is applied with the virtual, rotational stiffness c_r, so that $U_{\mathrm{tc},1}$, $U_{\mathrm{tc},2}$, $U_{\mathrm{rc},1}$ and $U_{\mathrm{rc},2}$ possess the same value for respective high deviation $\boldsymbol{e_r}$, $\boldsymbol{e_R}$, $\boldsymbol{e_n}$ and $\boldsymbol{e_m}$.

The final cost function is calculated by

$$e = \left\| \begin{pmatrix} U_{\mathrm{tc},1} & U_{\mathrm{tc},2} & U_{\mathrm{tr},1} & U_{\mathrm{tr},2} \end{pmatrix} \right\|_2^2, \tag{21}$$

The visualised example in Fig. 3 shows a result of the optimisation process with numeric integration from base to tip. The violet dot depicts the measured position at the tip and position at the base. Physical parameters are normalized regarding values calculated from literature to improve the conditioning of the optimisation problem. The resulting optimisation problem for the column vector $\boldsymbol{\sigma}$ containing the scaling factors is formulated by

$$\begin{pmatrix} \sigma^*_\mathrm{ext.} & \sigma^*_{\mathrm{bend.},x} & \sigma^*_{\mathrm{bend.},y} \end{pmatrix}^\mathrm{T} = \underset{\boldsymbol{\sigma}\in\mathbb{R}^3}{\arg\min}\, e(\boldsymbol{\sigma}). \tag{22}$$

If some initial conditions of the shooting method are unknown, they are added to the set of optimisation parameters. In the following, the regression method for prediction of scaling factors is presented.

C. Artificial Neural Network

The identified pressure-dependent stiffness parameters are used to learn the relationship between actuating pressures and resulting stiffness parameters. We set up an artificial neural network (ANN) for each element of the scaling vector $\boldsymbol{\sigma}$ as

$$\sigma_\mathrm{ext.} = f_{\mathrm{ANN,ext.}}(\boldsymbol{p}) \tag{23}$$

$$\sigma_{\mathrm{bend.},x} = f_{\mathrm{ANN,bend.},x}(\boldsymbol{p}) \tag{24}$$

$$\sigma_{\mathrm{bend.},y} = f_{\mathrm{ANN,bend.},y}(\boldsymbol{p}). \tag{25}$$

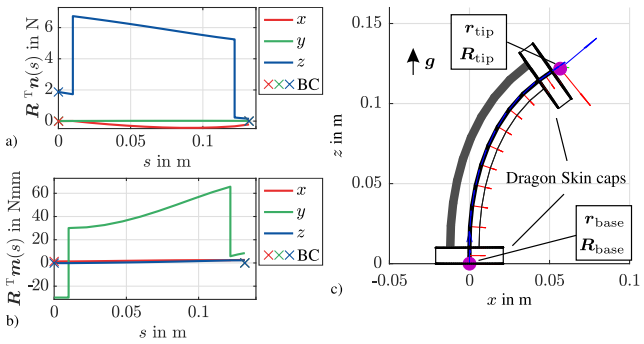

Fig. 3. Optimisation result for a single static state using the proposed cost function. The boundary conditions are shown as crosses in the plots a) distributed body forces and b) body moments and violet dots as well as directors in c)

TABLE II
ARTIFICIAL NEURAL NETWORK PARAMETERS FOR LEARNING THE PRESSURE TO STIFFNESS RELATIONSHIP

parameter	value
feedforward neural network architecture:	
number of input neurons	3
number of output neurons	1
number of neurons hidden layer 1	45
number of neurons hidden layer 2	50
activation function hidden layer 1	$\tanh(v)$
activation function hidden layer 2	$\tanh(v)$
activation function output layer	v (linear)
training parameters:	
relative size training set	80 %
relative size validation set	20 %
maximum number of epochs	100
early-stopping	10
optimisation method Levenberg-Marquardt with Bayesian regularisation:	
initial value	0.01
increase factor	10
decrease factor	0.1
maximum value	10

The three multilayer perceptrons are set up with the hyperparameters shown in Table II. For optimising the network's parameters (weights and biases) we choose the Levenberg-Marquardt backpropagation algorithm with Bayesian regularisation. The algorithm not only minimises the mean squared error between target values (i.e. identified scaling factors) and network output, but simultaneously minimises the network's weights, in order to give the learned function a degree of smoothness and generalise well over unseen data [19]. The learned continuous mapping can be used in a hybrid model, which combines the classical mechanical Cosserat rod model and a data based actuation - stiffness map.

IV. EXPERIMENTAL SETUP

Fig. 4 shows the experimental setup. The soft actuator is fixed to a metal frame facing downwards. The three pressure chambers of the actuator are each connected to a proportional valve (LS-V25s, Enfield Technologies) via silicone tubes. The test stand runs with a pressure supply of 200 kPa.

Sensors: The valves' outputs are connected to a pressure sensor (142BC30A-PCB, First Sensor) each to enable PID control of the pressure within the chambers [18]. Cameras (Prime 17W, OptiTrack) used for optical tracking of the actuator's tip are connected to an external computer via Gigabit Ethernet. Tracking markers are attached to the actuator's tip to allow for position and orientation tracking. Base reaction forces are measured using a 6-axis force/torque sensor (Nano17, ATI Industrial Automation).

Signal processing: Pressure sensor inputs and valve commands are read in and set via the EtherCAT realtime bus with input and output terminals (EL3164 and EL4104, Beckhoff). A Linux PC running a realtime kernel with the Preempt-RT patch hosts the pressure control process. Output voltages

This is the author's version of an article that has been published in the IROS 2021 proceedings.
Changes were made to this version by the publisher prior to publication.
The final version of record is available at https://doi.org/10.1109/IROS51168.2021.9636447

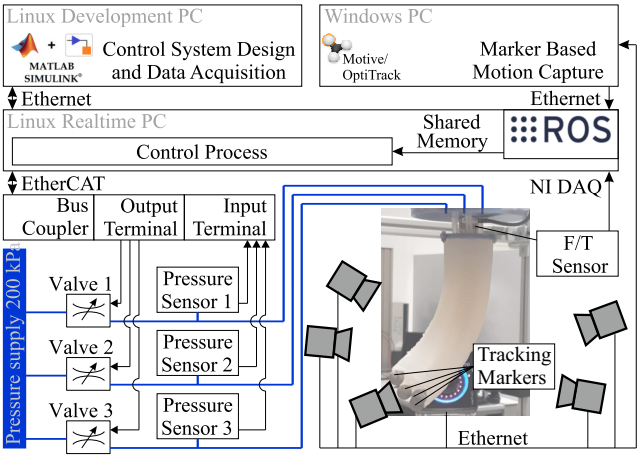

Fig. 4. Test bench for the analysis of a soft pneumatic actuator. Each actuator chamber is connected to a valve and a pressure sensor to allow seperate pressure control for each chamber. A camera system tracks the SPA's end effector position. Base reaction forces are measured using a 6-axis force/torque sensor. The actuator system is controlled with a realtime Linux PC.

are set according to the PID control system for controlling the valves. The OptiTrack software Motive processes the camera data on a Windows PC and streams position and orientation data to the realtime PC via Ethernet. A ROS Node processes this data and provides the pose to be saved. The output of the force/torque sensor is connected to a data acquisition card (NI6220, National Instruments) within the realtime PC. There, using a calibration matrix, the output voltages are converted to forces and torques which are further processed with an interface based on the `nidaqmx` library. This general interface may be used for any sensor voltage readings compatible with NI I/O cards. Offset correction is carried out during the initial straight configuration of the soft actuator, such that all forces and torques are zeroed out except for the force in z-direction which is calibrated to give a signal according to the actuator's mass (including markers).

The control architecture and data acquisition described above is set up in MATLAB/Simulink using the Etherlab framework on an external development PC and compiled to run on the realtime PC. With this set up we can obtain the required data, namely chamber pressures and the corresponding actuator's tip position and orientation as well as the base reaction forces and torques at each time step with a sample time of 1 ms.

V. VALIDATION AND DISCUSSION

In order to validate the proposed identification and hybrid modelling approach, a dataset of $21^3 = 9261$ samples is generated by screening the actuator space in steps of 3.5 kPa from 0 to 70 kPa in each chamber. Pressure is given as difference of measured and atmospheric pressure.

A. Identification

In this first study we apply the proposed identification procedure for each sample by numerically integrating from tip to base, with known boundary conditions $\boldsymbol{r}_{\text{tip}}$ (measured) and $\boldsymbol{m}_{\text{tip}} = \boldsymbol{0}$. The tracking markers at the actuator's tip are considered a point mass of $m_{\text{marker}} = 6\,\text{g}$ and accounted for in the boundary condition $\boldsymbol{n}_{\text{tip}} = m_{\text{marker}}\boldsymbol{g}$. For the residual at the actuator's base, the position and orientation are known. The dataset for identification therefore only contains the actuation pressure and the respective measured tip position of the soft actuator.

Fig. 5 depicts these tip positions with the colour indicating the identified scaling factor for the corresponding stiffness parameter σ. Samples, for which the identification algorithm is unable to find a solution, are excluded from the visualisation, validation and further processing during neural network training. This failure in identification can be observed if the deformed state lies near the principal axes of the undeformed cross section.

Small deformations in x result in small flexural strains u_y, so that the bending stiffness around y has not sufficient impact on the model's behaviour in this point, thus no valid parameter is identified. The same applies for a deformation along the y-axis and bending stiffness around x.

Fig. 5 shows that the identified scaling factor for the longitudinal stiffness $\boldsymbol{\sigma}_{\text{ext.}}$ is below 1 throughout the actuator's workspace. This means the actual stiffness is lower than the ideal geometrical data in combination with literature material parameters suggests. Moreover, the more deformation the actuator exhibits, the higher the identified longitudinal stiffness becomes.

The identified scaling factors for bending stiffnesses $\boldsymbol{\sigma}_{\text{bend.},x}$ and $\boldsymbol{\sigma}_{\text{bend.},y}$ both range from around 0.4 to 1.4 with $\boldsymbol{\sigma}_{\text{bend.},y}$ being slightly higher. A tendency is visible that with increasing elongation a softening of the bending stiffness occurs. Besides a nonlinear stress - strain relationship, this behaviour might be due to a volume preserving constriction of the cross section, thus a decrease of the second moment of area.

The identified parameters are validated with their related actuation pressures in forward simulations from base to tip with known base position $\boldsymbol{r}_{\text{base}}$ and orientation $\boldsymbol{h}_{\text{base}}$ and the tip force and moment ($\boldsymbol{n}_{\text{tip}}$ and $\boldsymbol{m}_{\text{tip}}$) for the residual, as it is described in Sec. II. The mean absolute position error w.r.t. the initial actuator length over all remaining samples is less than $9{\cdot}10^{-6}\%$, showing the effectiveness of the identification method. Since these parameters are not directly used in the model, which is done with trained ANN and described in the next section, a validation on a separated test set of data is not intended.

B. Scaling Factor Learning

For the subsequent training of the neural networks, the dataset is separated in 80% for training and 20% for validating. Only the successfully identified pressure - scaling factor data pairs are selected to be used in the actual training and neural network performance analysis.

The box plot illustrated at the top of Fig. 6 shows the deviation between ANN output and target data for the individual scaling factors. While the majority of errors is

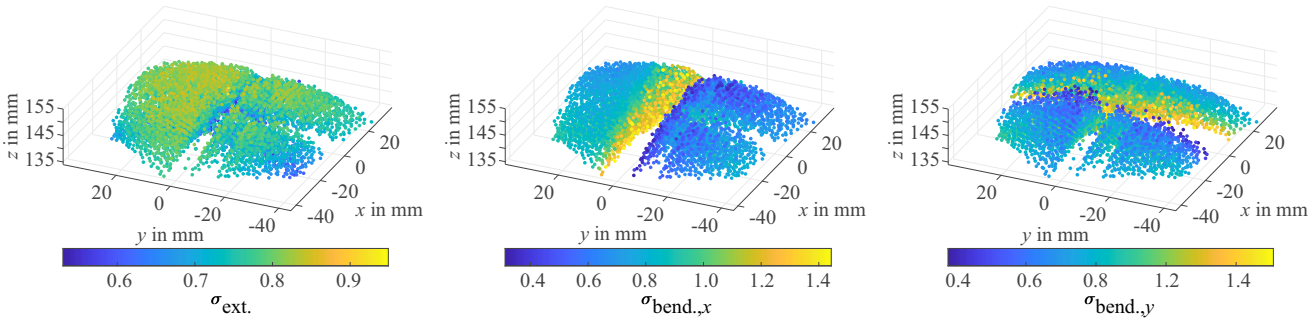

Fig. 5. Measured tip positions of the SPA depending on different pressure inputs. The colour codes indicate the identified scaling factor for the respective stiffness parameter in that operating point.

distributed closely around 0, the maximum error is around 300%. Depicting the errors according to the corresponding tip position as done exemplarily in the bottom of Fig. 6 for $\sigma_{\text{bend.},x}$ reveals that the larger errors occur when the tip position lies close to the principal x-axis.

As mentioned earlier this is where the influence of the bending stiffness around x is minimal. Hence, the identification procedure is hardly sensitive to changes of $\sigma_{\text{bend.},x}$, which might lead to a undesired scattering behaviour of the identified scaling factor near the principal axis. The ANN does not reproduce this behaviour, thus shows large errors in prediction.

C. Hybrid Model

Finally, we validate the full hybrid modelling approach by applying the ANNs in forward simulation from base to tip. Therefore, all pressure - tip position data pairs from the test set are used including data pairs where no successful identification was carried out.

Fig. 7 shows the error between measured tip position and simulated tip position using the hybrid model. In the box plot, the radial distance Δr is given as the deformation in the x-y-plane, because it intuitively summarises the error Δx and Δy, while Δz is displaying the error in height of the tip position. Errors are reported as measured (or target) minus simulated value in relation to the initial actuator length of 130 mm. For comparison, the box plot also includes the errors when simulating the model with constant stiffness parameters taken from literature (indicated by subscript LIN).

Overall, simulation of the Cosserat model with a learned mapping from actuation to stiffness parameters shows good accordance with measured tip positions. The deformation in radial direction as well as in z-direction shows errors less than 2.2% when compared to measured tip positions (see Fig. 7). Note, that this includes operating points, the identification was not able to find a solution for. The ANN generalises well for unseen data. Although the performance analysis of the ANNs showed large errors when it comes to approximating the identified values, these errors do not occur in the error analysis of the hybrid model. This again indicates the weak influence of the bending stiffness when the SPA performs a deformation close to the principal axis.

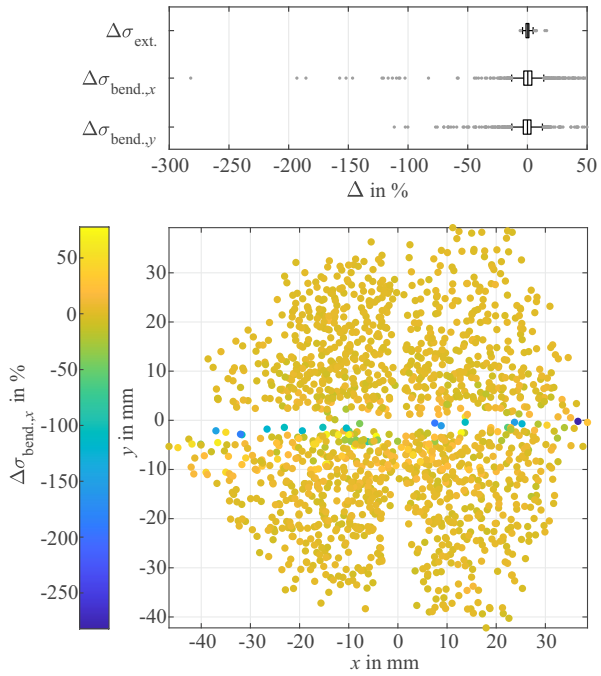

Fig. 6. Error between ANN output for scaling factors and identified factors (top). Error for $\sigma_{\text{bend.},x}$ visualised according to tip position (bottom). Large errors occur when the tip position is close to the principal x-axis.

In contrast to the hybrid model the linear elastic material parameters from literature overestimate the stiffness. The actual deformation of the actuator is greater than the simulated one in this case.

The mean relative Euclidean distance between simulation and measurements is 0.59% and thereby more than seven times lower than for simulations using linear elastic literature parameters (mean 4.26%). Standard deviations are 0.42% and 1.61%, respectively.

D. Discussion

The proposed hybrid modelling method was validated with a single actuator segment without external loads. Future work will target extrapolation considering external loads by e.g. attaching external payload or mounting the actuator sideways

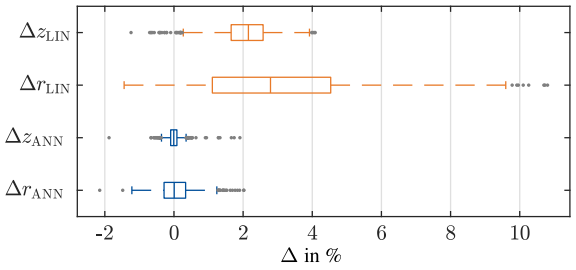

Fig. 7. Prediction errors in radial distance Δr with $r = \sqrt{x^2 + y^2}$ and height Δz of linear (LIN) Cosserat and hybrid (ANN) Cosserat model given in relation to the initial actuator length of 130 mm.

and validate and adapt the presented approach for multi-segment manipulators. This will likely increase the shear within the actuator, which calls for the identification of further parameters. Furthermore, it might be necessary to investigate the input of the ANN in order to generalize well.

Besides these additional scenarios, we will conduct further analyses incorporating all available sensor information namely base reaction forces and moments and tip orientation. Therefore, a suffient amount of data from experiments has to be collected to perform these evaluations.

VI. CONCLUSIONS

Geometrical and material nonlinearities are a challenging topic in soft material robotic research. We presented a hybrid modelling approach combining classical mechanical Cosserat rod modelling with data based stiffness estimation. Instead of nonlinear constitutive equations that have to be solved numerically, our model relies on a workpoint-dependent linear stress-strain relationship. Thus, we keep the modelling approach computationally efficient, in order to be used for static control, trajectory planning, design optimisation or be enhanced for dynamics modelling and control.

The presented identification method enables the incorporation of various sensor information at the actuator's ends and the identification of stiffness parameters for linear-elastic Cosserat rod models.

Experimental validation was carried out, by identifying longitudinal and bending stiffness of a soft pneumatic actuator and learning the actuation to stiffness map using artificial neural networks. The hybrid model was able to predict the tip position of the actuator given a pressure input with a mean error of 0.59%.

For future work, we will further analyze this hybrid modelling approach by investigating the influence of added payload on the accuracy and the applicability to multi-segment soft pneumatic manipulators. Besides offline identification and learning, an extension of the approach towards online learning is considered to keep up with effects like material fatigue. Moreover, we intend to enhance the approach to handle the system dynamics.

REFERENCES

[1] T. George Thuruthel, Y. Ansari, E. Falotico, and C. Laschi, "Control Strategies for Soft Robotic Manipulators: A Survey," Soft Robot., vol. 5, no. 2, pp. 149–163, 2018, doi: 10.1089/soro.2017.0007.

[2] M. T. Chikhaoui, J. Granna, J. Starke, and J. Burgner-Kahrs, "Toward Motion Coordination Control and Design Optimization for Dual-Arm Concentric Tube Continuum Robots," IEEE Robot. Autom. Lett., vol. 3, no. 3, pp. 1793–1800, 2018, doi: 10.1109/LRA.2018.2800037.

[3] J. Till, V. Aloi, and C. Rucker, "Real-time dynamics of soft and continuum robots based on Cosserat rod models," The Int. Jour. of Robotics Research, vol. 38, no. 6, pp. 723–746, 2019, doi: 10.1177/0278364919842269.

[4] D. Trivedi, C. D. Rahn, W. M. Kier, and I. D. Walker, "Soft robotics: Biological inspiration, state of the art, and future research," Applied Bionics and Biomechanics, vol. 5, no. 3, pp. 99–117, 2008, doi: 10.1080/11762320802557865.

[5] P. Polygerinos, N. Correll, S. A. Morin, B. Mosadegh, C. D. Onal, K. Petersen, M. Cianchetti, M. T. Tolley, R. F. Shepherd, "Soft Robotics: Review of Fluid-Driven Intrinsically Soft Devices; Manufacturing, Sensing, Control, and Applications in Human-Robot Interaction," Adv. Eng. Mater., vol. 521, no. 5, p. 1700016, 2017, doi: 10.1002/adem.201700016.

[6] A. D. Marchese and D. Rus, "Design, kinematics, and control of a soft spatial fluidic elastomer manipulator," The Int'l Journal of Robotics Research, vol. 35, no. 7, pp. 840–869, 2016, DOI: 10.1177/0278364915587925.

[7] D. Trivedi, A. Lotfi, and C. D. Rahn, "Geometrically Exact Models for Soft Robotic Manipulators," IEEE Trans. Robot., vol. 24, no. 4, pp. 773–780, 2008, doi: 10.1109/TRO.2008.924923.

[8] N. K. Uppalapati, G. Singh, and G. Krishnan, "Parameter estimation and modeling of a pneumatic continuum manipulator with asymmetric building blocks," in 2018 IEEE Int. Conf. on Soft Robotics (RoboSoft), Livorno, Italy, Apr. 2018, pp. 528–533, doi: 10.1109/ROBOSOFT.2018.8405380.

[9] H. B. Gilbert and I. S. Godage, "Validation of an extensible rod model for soft continuum manipulators," RoboSoft 2019 - 2019 IEEE Int. Conf. Soft Robot., no. 1718755, pp. 711–716, 2019, doi: 10.1109/ROBOSOFT.2019.8722721.

[10] V. Falkenhahn, T. Mahl, A. Hildebrandt, R. Neumann, and O. Sawodny, "Dynamic Modeling of Bellows-Actuated Continuum Robots Using the Euler–Lagrange Formalism," IEEE Trans. Robot., vol. 31, no. 6, pp. 1483–1496, 2015, doi: 10.1109/tro.2015.2496826.

[11] C. Della Santina, R. K. Katzschmann, A. Bicchi, and D. Rus, "Model-based dynamic feedback control of a planar soft robot: trajectory tracking and interaction with the environment," Int. J. Rob. Res., vol. 39, no. 4, pp. 490–513, 2020, doi: 10.1177/0278364919897292.

[12] S. M. H. Sadati, S. E. Naghibi, A. Shiva, I. D. Walker, K. Althoefer, and T. Nanayakkara, "Mechanics of Continuum Manipulators, a Comparative Study of Five Methods with Experiments," 2017, pp. 686–702, doi: 10.1007/978-3-319-64107-2_56.

[13] S. Grazioso, G. Di Gironimo, and B. Siciliano, "A Geometrically Exact Model for Soft Continuum Robots: The Finite Element Deformation Space Formulation," Soft Robot., vol. 6, no. 6, pp. 790–811, 2019, doi: 10.1089/soro.2018.0047.

[14] T. G. Thuruthel, B. Shih, C. Laschi, and M. T. Tolley, "Soft robot perception using embedded soft sensors and recurrent neural networks," Sci. Robot., vol. 4, no. 26, 2019, doi: 10.1126/SCIROBOTICS.AAV1488.

[15] S. S. Antman, "Nonlinear Problems of Elasticity", vol. 107. New York, NY: Springer New York, 1995, 10.1007/0-387-27649-1.

[16] C. Rucker, "Integrating Rotations Using Nonunit Quaternions," IEEE Robot. Autom. Lett., vol. 3, no. 4, pp. 2979–2986, 2018, doi: 10.1109/LRA.2018.2849557.

[17] C. Hertzberg, R. Wagner, U. Frese, and L. Schröder, "Integrating generic sensor fusion algorithms with sound state representations through encapsulation of manifolds," Inf. Fusion, vol. 14, no. 1, pp. 57–77, 2013, doi: 10.1016/j.inffus.2011.08.003.

[18] S. Ibrahim, J. C. Krause and A. Raatz, "Linear and Nonlinear Low Level Control of a Soft Pneumatic Actuator", IEEE Int. Conf. on Soft Robotics (RoboSoft), Seoul, Korea (South), 2019, pp. 434–440, doi: 10.1109/ROBOSOFT.2019.8722737.

[19] F. Dan Foresee and M. T. Hagan, "Gauss-Newton approximation to Bayesian learning," Int. Conf.on Neural Networks (ICNN'97), Houston, TX, USA, 1997, pp. 1930-1935, doi: 10.1109/ICNN.1997.614194.